New Design approach for a highly loaded Counter-Rotating Mixed-Flow Pump in Cavitation Conditions

S. Tosin - J. Friedrichs

A. Dreiss

Institute of Jet Propulsion
and Turbomachinery,
Technische Universität Braunschweig
38108 Braunschweig, Germany
Email: s.tosin@ifas.tu-bs.de

Flowserve Corporation
Hamburg, Germany

ABSTRACT

The ongoing research on counter-rotating blade rows in single stage machines has shown promising results on improvement of efficiency and pressure ratios in high specific speed impellers, with conventional applications such as naval propulsion etc, axial pump and fan. The focus of the design presented below has been the development of a compact design with high power density and improved cavitation performance. The new design offers a downsizing opportunity with its two impellers: a mixed-flow front rotor (FR) and the radial rear rotor (RR), instead of a stationary bladed diffuser. With this set the off-design working range can be extended, reaching a high adaptability at different flow conditions. An improvement on cavitation's performance can be obtained also moving the load from the FR to the RR. In this paper the first prototype is numerically and experimentally analyzed. Head drop and cavitation inception curves besides the characteristic curves are highlighted. Design improvements have finally permitted to develop two new versions of the FR, which have been numerically investigated. The first one is expected to provide improved cavitation performance, while the second one higher power density. Finally the sensitivity of the system to the speed ratio has been experimentally investigated. The CFD results show good agreement with the tests within the uncertainty of the experimental measurements.

KEY WORDS

Cavitation, Counter-Rotating, Power Density, Compact, Centrifugal Pump, Mixed-Flow

INTRODUCTION

A new pump design concept based on counter-rotating impellers has been analyzed in this paper. The aim of this research is to investigate the possibility to downsize the machine and achieve a compact unit with a broad working range by introducing an additional counter-rotating radial impeller downstream of a mixed-flow runner. This paper follows the previous study (Tosin, 2014 [9]), highlighting the performance analysis done on the first prototype called $RoDiff_1$ and giving a brief introduction on the following prototypes. The design model developed in house and widely presented within the mentioned paper has been improved by adding more design features and options, which have permitted the authors to get $RoDiff_2$ design. Moreover the second prototype has been designed to improve the cavitation performance focused on the inception cavitation. A third one $RoDiff_3$, which reaches a higher power density, is also introduced to show importance of the load distribution between front and rear rotor. The definition of the power density used in the present study is: $\rho_P = \frac{P}{\frac{\pi \cdot \rho_{imp} D_4^2 \cdot Z_{0,4}}{4 \cdot 2}}$ where the shaft power in counter-rotating system consists of the addition

1

of both shaft powers. Various designs by the counter-rotating principle are available in literature; many authors have investigated this innovative layout applied to axial-flow machines. Literature survey introduced some interesting publications on this concept. Notably Kanemoto et al. (2004 [4]) presents axial flow pump with counter-rotating impellers driven by a single electric motor with counter-rotating rotors. The study of Momosaki et al. (2010 [5]) highlights performance of an axial arrangement with a Front Rotor and Rear Rotor investigating the flow field with CFD analysis. The results of Shigemitsu (2007 [7]) show some benefits on static head rise in comparison with the conventional rotor-stator configuration without causing losses in terms of total efficiency. Looking into the recent publication, two interesting works could be found about this topic. From the University of Kyushu an experimental investigation of the blade row interactions in counter-rotating axial flow pump have been carried out (Cao et al., 2014 [2]). The work shows the results of pressure pulsation measurements in different location within the bladed channel, producing a model for the prediction of the fluctuation modes, which was tested for two rotational speed combinations. The paper of Wand et al. (2014 [10] from Dynfluid Laboratory ParisTech) presents a design parameter sensitivity analysis based on experimental investigation in a counter-rotating axial flow fan. The interaction of the rotors and the determination of the most important design parameters have been the objectives of the authors. Both papers have given the basis for the improvements of the existing version of the design tool internally developed, that was presented in the previous publication. The actual version of the design software is able to design in single rotor layout, conventional mixed-flow and radial-flow impellers. Once the counter-rotating layout is set, it can design simultaneously both counter-rotating impellers, in this case the axial and radial extension, the speeds, the head rise and many other parameters for each rotor are freely set from the user. The present study uses the same simulation setup that
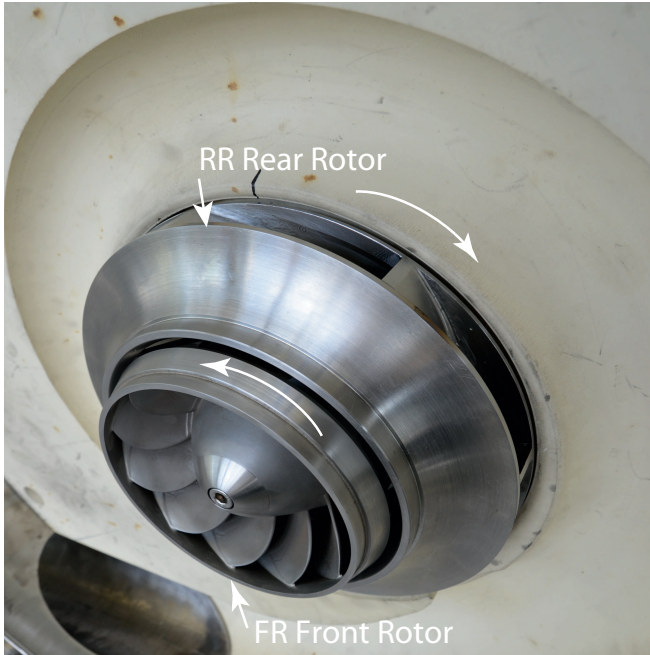

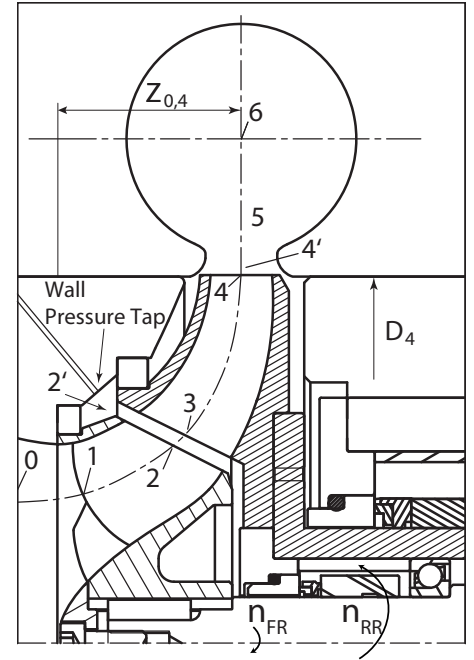Figure 1: **Picture of the impellers in the test rig**

Figure 2: **Meridional section (Tosin, 2014 [9])**

was widely described in the previous paper (Tosin, 2014 [9]) and therefore the simulation setup will be briefly introduced in the NUMERICAL SETUP part.

EXPERIMENTAL SETUP

In Figure 1 the counter-rotating impellers can be observed, the half of the spiral duct made of PVC and the brass ring seals support have been disassembled from the test rig to permit the optical access. The design concept, which has been proposed in the following pages, is based on replacing

the diffuser with a counter-rotating impeller, keep on adding energy to the fluid by a bladed rotating diffuser. From here comes the name of the prototype series RoDiff which stands for Rotating Diffuser. An additional stationary diffuser after the radial impeller could be foreseen, but it wasn't considered for the actual analysis. This new layout increases the entire machine power density and the machine becomes more compact. Furthermore the additional degree of freedom offered from the speed of the second rotating runner permits to better optimize the performance outside the BEP.
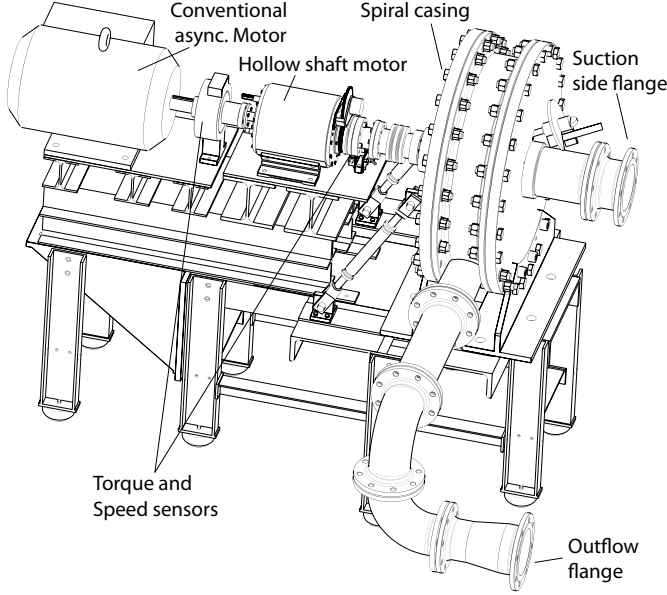

Figure 3: **3D Model of the Test Rig**

Figure 2 reports a meridional section of the hydraulics and Figure 3 shows schematically the entire test rig. Two independent asynchronous motors are used to run the impellers, their speed are independently controlled. The machine setup (showed in Figure 2) consists of an inner shaft connected to the front rotor (FR), runs through the outer shaft connected to the rear rotor (RR) spinning with opposite direction. The RR is connected to the shaft by a connection disk rigidly fixed on the outer shaft which simplifies the assembly. The points from 0 to 6 indicate in Figure 2 locations used as reference planes. The n_{FR} and n_{RR} define the rotational speeds respectively. Between each impeller and the motor (not shown in Figure 2) there are elastic couplings, torque and speed sensors. Both motors are individually controlled through an inverter within a speed range of 0 to 3000 rpm. The outer shaft is connected to a hollow-shaft electric motor, specifically designed and assembled within the institute facilities. The inner shaft is run by a standard asynchronous motor. The pump has a single volute casing with circular cross section and it is inserted in a closed system water test-circuit composed by: a tank, a main valve, a by-pass valve and an additional auxiliary pump to test also for overload conditions. The outflow section is connected to a DN125 mm flange, the suction section instead is connected to the DN150 mm. Some visual access points are also available. During the cavitation measurements the system can run up to an absolute pressure of 20 kPa by pumping water out of the tank and so causing the reduction of the pressure inside the circuit. Due to mechanical and structural limitations the maximal pressure could be increased until 650 kPa. During the characteristic curve measurements the entire system is pressurized up to a relative pressure of 150 kPa to avoid the cavitation phenomena in part-load working condition. The measurements have been conducted following the European Norm EN ISO 9906:2012 and the most relevant definitions are reported below:

$$H_{TT} = \frac{p_{5t} - p_{0t}}{\rho g} \qquad (1)$$

$$H_{FR} = \frac{p_{2't} - p_{0t}}{\rho g} \qquad (2)$$

$$H_{RRVO} = \frac{p_{5t} - p_{2't}}{\rho g} \qquad (3)$$

$$\eta_T = \frac{\rho Q H_{TT} g}{M_{FR} \cdot \omega_{FR} + M_{RR} \cdot \omega_{RR}} \qquad (4)$$

$$NPSH_A = \frac{p_{0t} - p_v}{\rho g} \qquad (5)$$

$$NPSH_{ic} = \frac{p_{0t} - min(p_s)_{Volume}}{\rho g} \qquad (6)$$

The test rig is basically a double motor block with a spiral duct realized in PVC, hosted in a steel chamber. The measurement system is composed of a magnetic volume-flow transducer, several relative diaphragm pressure sensors, speed and torque sensor one per each impeller. The main characteristics and the instrument measurement uncertainty is given in the Table 1.

Table 1: Characteristics and Sensor Uncertainty of the measurement system

Sensor Type	Magnitude	ϵ_r	Range
Relative Pressure sensor Inflow - Atm	$p_s, atm0$	0.5%	$0 - 3.5bar$
Relative Pressure sensor FR-Outlet - Inflow	p_m, s	0.5%	$0 - 1.7bar$
Relative Pressure sensor Outlet - Inflow	p_d, s	0.5%	$0 - 5bar$
Inductive Volume-Flow flow-meter	Q	0.5%	$0 - 600m^3/h$
Inductive Speed Sensor FR	n_{FR}	1.0%	$0 - 3000rpm$
Inductive Speed Sensor RR	n_{RR}	1.0%	$0 - 3000rpm$
Torque Sensor FR	M_{FR}	0.2%	$0 - 100Nm$
Torque Sensor RR	M_{RR}	0.2%	$0 - 200Nm$
Temperature Probe	T	0.8%	$0 - 100\ C^o$

SIMULATION SETUP

CFD investigations have been applied throughout the project to analyze and improve the prototypes. The numerical setup is basically the same used in the previous study of the same system already published (Tosin, 2014 [9]). Figure 4 presents the simulated volume composed by four blocks: the inflow, FR with 11 blades and spinning anti-clockwise, the RR with 7 blades spinning clockwise, and the spiral duct. All the results shown below are actually solved in steady state analysis. The time averaged values from the unsteady analysis actually provide great agreement with those from the steady state runs, see [9]. The mesh consists in $12 \cdot 10^6$ nodes and the maximum Y+ value on the blade's surfaces is less than 2. The physical time step has been set to $5 \cdot 10^{-5}s$ after a simulation convergence study.

The previous results of the mesh independency study have been taken to define the node number and the in house simulations were carried out on a cluster with 4 nodes and 16 CPUs each. Different from the previous study, during the cavitation analyses, the machine is simulated as full model with all blades and no periodicity conditions. The interface between the rotors is a standard mixing-plane (stage) with a velocity average criterion, and the solver used is ANSYS CFX (2013 [1]). The usage of the full model was necessary to run the cavitation analysis with two rotating domains due to the asymmetry of the volute inflow pressure distribution in off-design conditions. The fluid model is water-liquid at 25°C and in case of cavitation analysis, water-vapor at 25°C is combined according to the Rayleigh-Plesset model, which is defined in CFX in the multiphase framework as an interphase mass transfer model. In this investigation the model parameters have

Figure 4: **Simulation 3D-Domain**

been left as default with saturation pressure of 3169.9 Pa. The turbulence model is Shear Stress Transport (SST) and high resolution scheme was chosen, which gives a good balance between calculating speed and accuracy. Moreover another main parameter with a high influence on the convergence profile is the number of blade: if the number of blade of both runners would be equal, a phenomena called clocking takes place. The pressure pulsations, generated at the blade passing frequency, cause an instability of the numerical method.
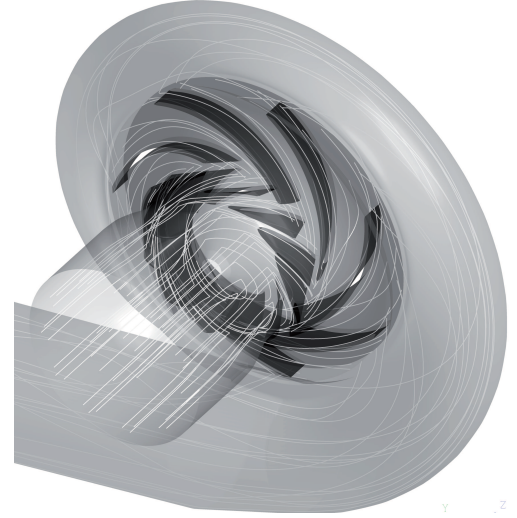
EXPERIMENTAL RESULTS: CHARACTERISTIC CURVES OF $RoDiff_1$

Figures 5 and 6 report the results of the experimental investigation on $RoDiff_1$. The dashed lines show the numerical results, it could be seen a good agreement between the CFD and EXP for the entire
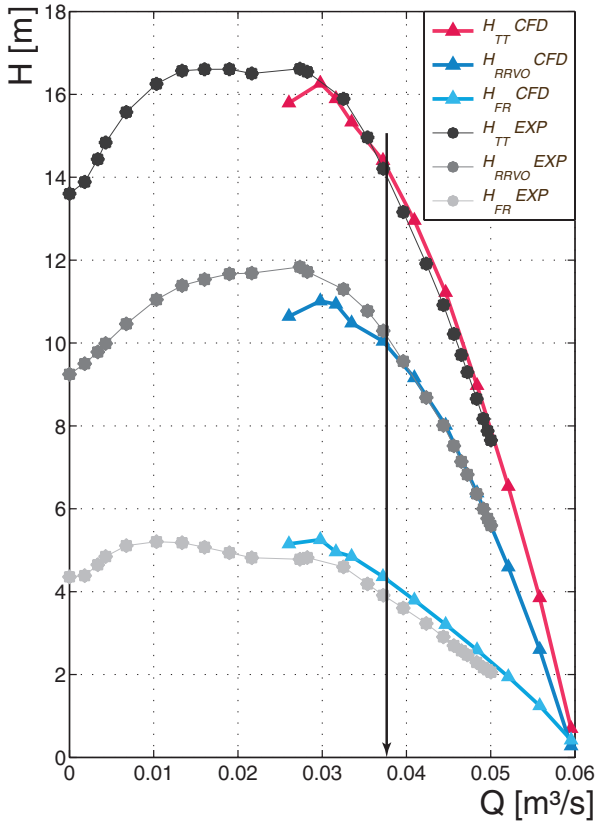
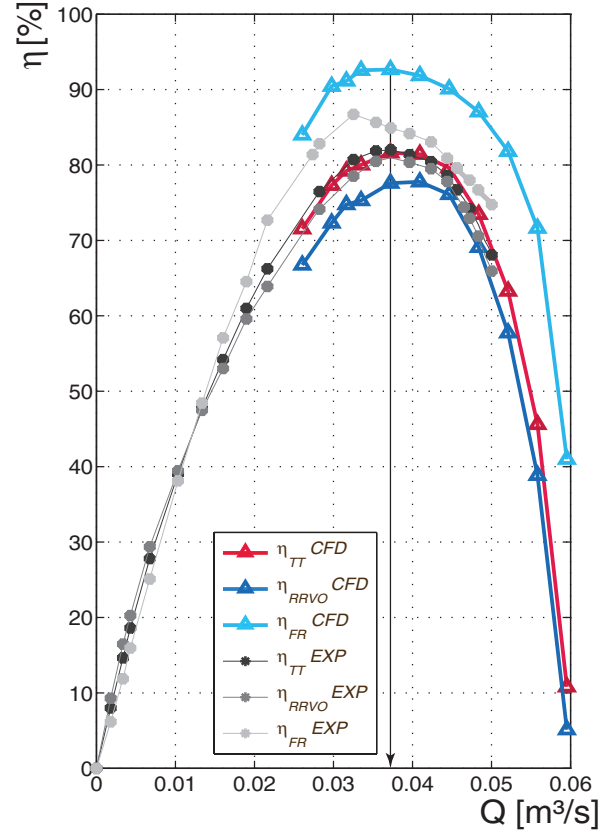Figure 5: **Comparison of Characteristic head curves CFD - EXP**

Figure 6: **Comparison of Characteristic efficiency curves CFD - EXP**

machine, although some differences are displayed at the head rise and efficiency curves of each rotor separately H_{FR} and H_{RRVO}. The experimental underestimation of the FR efficiency η_{FR} is caused by an inaccuracy of the measurement method used to get the total pressure value in the gap between the runners. Since the total pressure $p_{2't}$ can not be directly measured without a probe, the CFD tangential component of the absolute velocity at location 2' has been combined to the experimentally evaluated meridional component and finally they have been added as dynamic pressure to the static wall pressure $p_{2's}$. This approximation might be the cause of the mismatch. At the actual project status velocity measurements with 3 or 5 hole probes are planned for the next research phase. The CFD head curve matches very well with the experimental results, as well as the partial head H_{FR} and H_{RRVO}. When observing the efficiency curve, it has to be reminded that the comparison between CFD and EXP could only be done in terms of hydraulic efficiency, so that the mechanical losses of the system had to be measured. The authors have carried out for this purpose a no-load measurement at design speed without impellers. The water circuit was closed in order to run the motors and the sealing system, which needs to be plunged in water. For the no-load measurements some important assumptions must be made. The friction losses on both ring-sealing at the shroud side are assumed negligible and the bearing friction coefficient doesn't change due to the axial trust produced while the impellers are rotating. All these losses can't be also exactly distributed between the shafts, causing part of the mismatch on the efficiency curve for η_{FR} and η_{RRVO} shown at Figure 6. Beside of that, the machine head H_{TT} presents a positive slope at very low capacity which could be easily solved varying the speed ratio, as will be demonstrated in the following chapter. Between the 30% of Q and the BEP the head is almost constant and the maximum efficiency $\eta_{TTmax} = 83\%$ is reached exactly at the design point marked with the continuous line in Figure 6. Finally observing the CFD values, the low discharge is not reported, because the numerical method has been unstable and no clear convergence could be reached with the previous CFD setup.
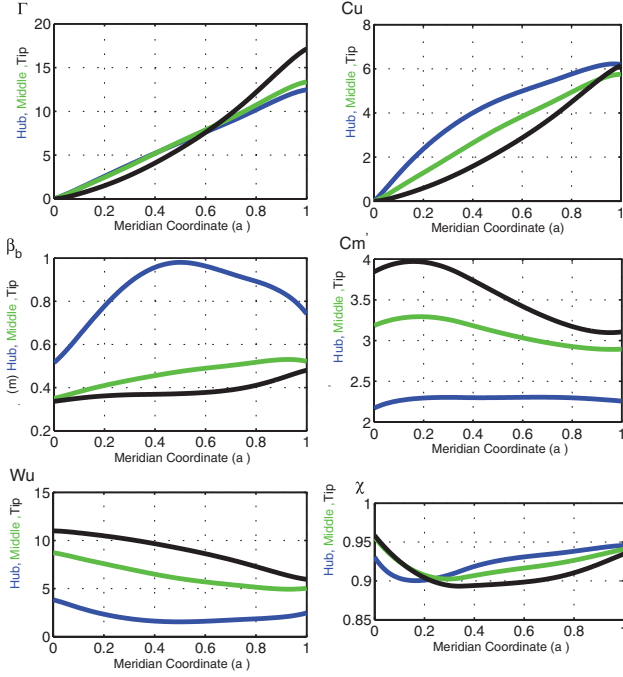
RE-DESIGN OF THE FRONT ROTOR

Figure 7: **Design Parameters: Circulation** Γ **, Meridional absolute velocity** C_m**, Tangential absolute velocity** C_u**, Tangential relative velocity** W_u**, Blade angle** β_b**, Obstruction factor** χ

After the first measurements on prototype $RoDiff_1$ of the characteristic curves and the NPSH curves, a second prototype $RoDiff_2$ has been developed in order to improve the cavitation behavior of the machine. For this purpose just the FR was re-designed due to the higher influence to the cavitation characteristics, keeping the rest of the system unchanged, with same volute and RR. The goal of the new design is mainly the improvements of the cavitation inception curve around BEP and the reduction of the $NPSH_{3\%}$. The experimental NPSH-curve is given in Figure 15 in chapter NUMERICAL AND EXPERIMENTAL CAVITATION ANALYSIS. The previous design tool has been modified to make it capable to accept the meridian velocity profiles coming from measurements or CFD as input and the thickness distribution is now added orthogonally to the zero-thickness blade surface, which allows asymmetrical thickness distribution. Having a look at Figure 8 the meridional PS and SS blade sections are plotted, according to the Kaplan method [3]. Those splines generated by the intersection of a meridian plane with the blade surface are cal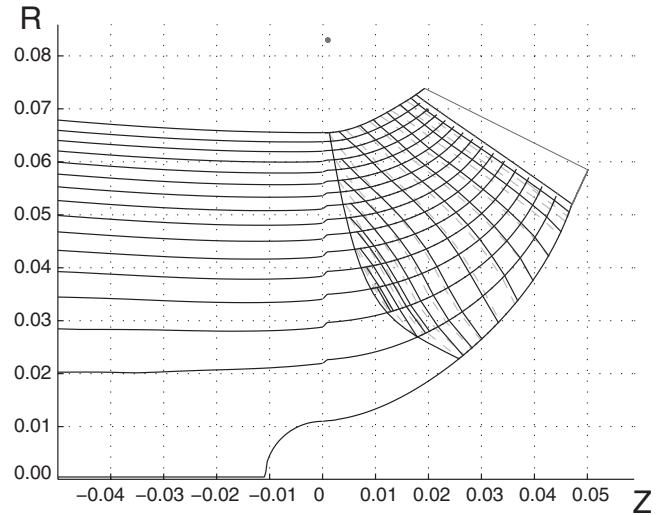culated after the design and they have been used to analyze the PS and SS surface in terms of local curvature, during the design phase. Finally the rotational speed was increased and the number of blades was reduced from 11 to 10. Blade angle distribution was adjusted to reduce the blade loading close to LE and the elliptical LE thickness distribution was made thinner.

Looking at Figure 7 the reduction of the tip blade loading at LE can be identified on the circulation distribution plot. The results of the previous publication [9] have shown that for this kind of machines the increase of the power density is one of the main advantages which this design offers and one of the most important design parameters seems to be the load distribution factor. This parameter is defined by the ratio $\chi_H = \frac{H_{RR}}{(H_{FR}+H_{RR})}$. With the aim to investigate the effect of this parameter to the pump performance a successive geometry $RoDiff_3$ has been developed with a higher FR speed and a lower load distribution factor. This new layout presents a FR speed of $2500rpm$ instead of $1600rpm$ and the number of blades is 9 instead of 11. The load distribution factor falls from 0.77 to 0.5. Basically this impeller has been designed to increase the entire head rise and to reach higher power density. Based on the numerical results this value is raised from $\rho_{P,1} = 2350[W/kg]$ to $\rho_{P,3} = 3650[W/kg]$. At this point of the research just the characteristic curves at design speed are available, while the experimental investigations on $RoDiff_2$ and $RoDiff_3$ are still in progress.
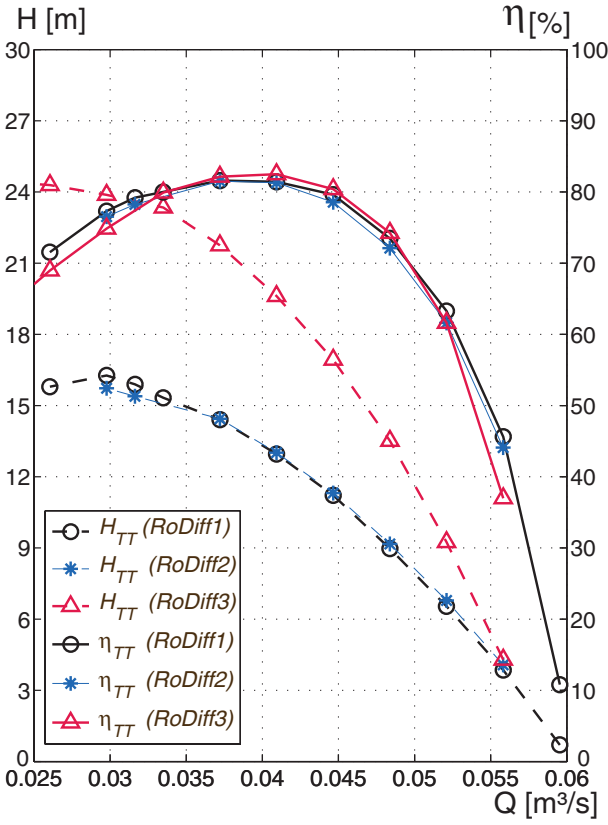

Figure 8: **Meridional Plane of** $RoDiff_2$

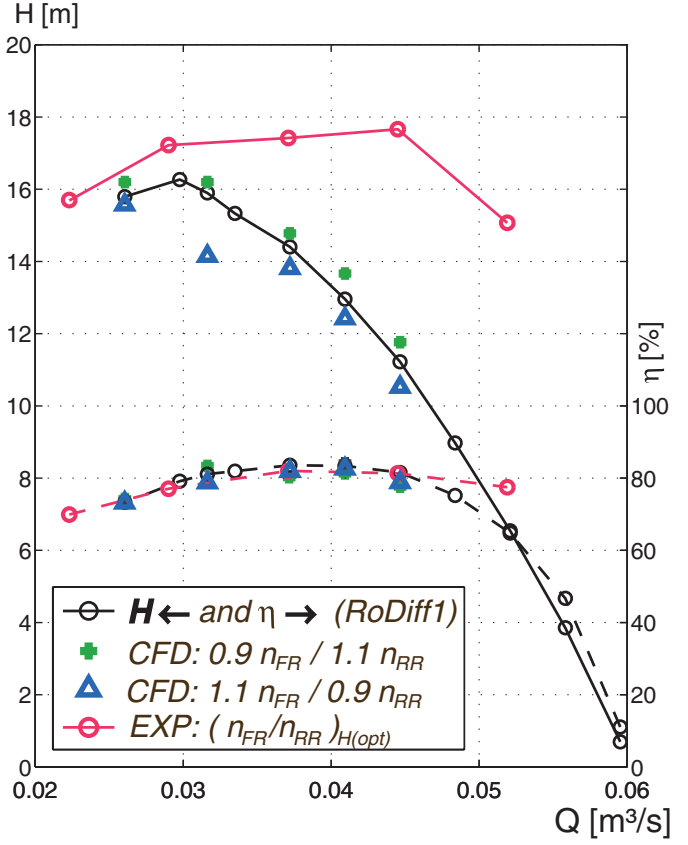Figure 9: **Characteristic curve comparison**

Figure 10: **Speed Ratio Sensibility analysis**

As already introduced the power density of the $RoDiff_3$ is higher than the previous prototypes, as observed on Figure 9. Basically within the same volute more energy is given to the fluid. The $RoDiff_2$ shows almost the same characteristic of $RoDiff_1$, while its improved cavitation performance could be seen at Figure 15. The authors note that in all three cases, the volute, the RR and its rotational speed are the same, and changes have been carried out just on the FR design. On Figure 10 the results of the speed ratio sensitivity study are reported. This analysis has been done experimentally as well as numerically. The speed ratio has been varied slightly and two characteristic curves have been simulated, plotted with the triangle and cross symbols. The experimental black line shows 5 working points in which the speed ratio has been iteratively optimized without varying the summation of both speeds, the resulting speed ratio is also shown in Figure 11. The speed ratio optimization done per each flowrate appears to be more effective and each working point offers several performance maximum, so that an objective function needs to be assumed. For example for the actual test the head rise has been maximized keeping the efficiency at the same or higher values measured in design speed ratio. This approach seems to be the way
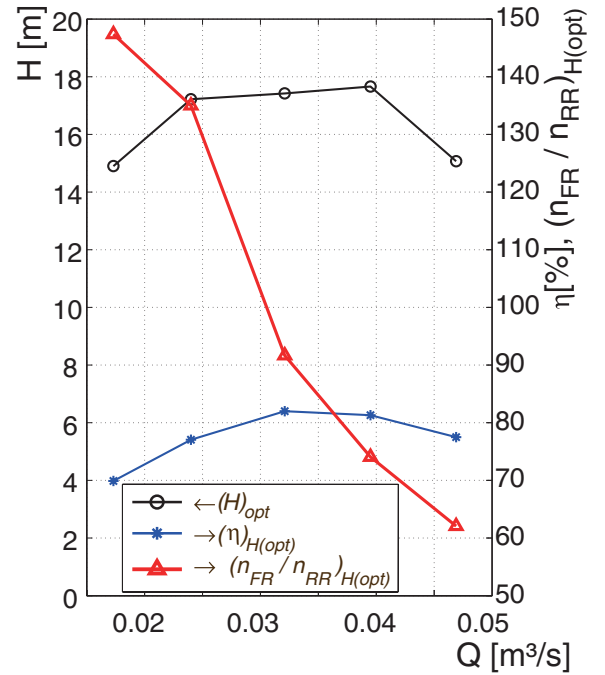

Figure 11: **Speed optimization** $RoDiff_1$

to realize a wide working range with almost constant head rise, as mentioned above. The optimized speed ratio values are also reported in Table 2.

Table 2: Speed ratio optimization test results

Q $[m^3/s]$	n_{FR} $[rpm]$	n_{RR} $[rpm]$	η_{TT} $[-]$	H_{TT} $[m]$	$n_{FR}+n_{RR}$ $[rpm]$	$\frac{n_{FR}}{n_{RR}}$ $[-]$
0.0223	1680	1140	0.699	14.90	2820	1.4737
0.0290	1620	1200	0.771	17.22	2820	1.3500
0.0371	1320	1440	0.820	17.42	2760	0.9167
0.0445	1200	1620	0.813	17.66	2820	0.7407
0.0519	1080	1740	0.775	15.07	2820	0.6207

NUMERICAL AND EXPERIMENTAL CAVITATION ANALYSIS

The vapor volume friction at three different $NPSH_A$ values are outlined in the CFD flow visualization at Figure 12. The plots b) and c) show a fast expansion of the vapor volume friction, while reducing the inlet total pressure of less than 5%. Experimental results are still not available to make a clear comparison with the CFD results. The numerical cavitation analysis on $RoDiff_1$ has been carried out during the development of the improved design $RoDiff_2$. The results highlight that the
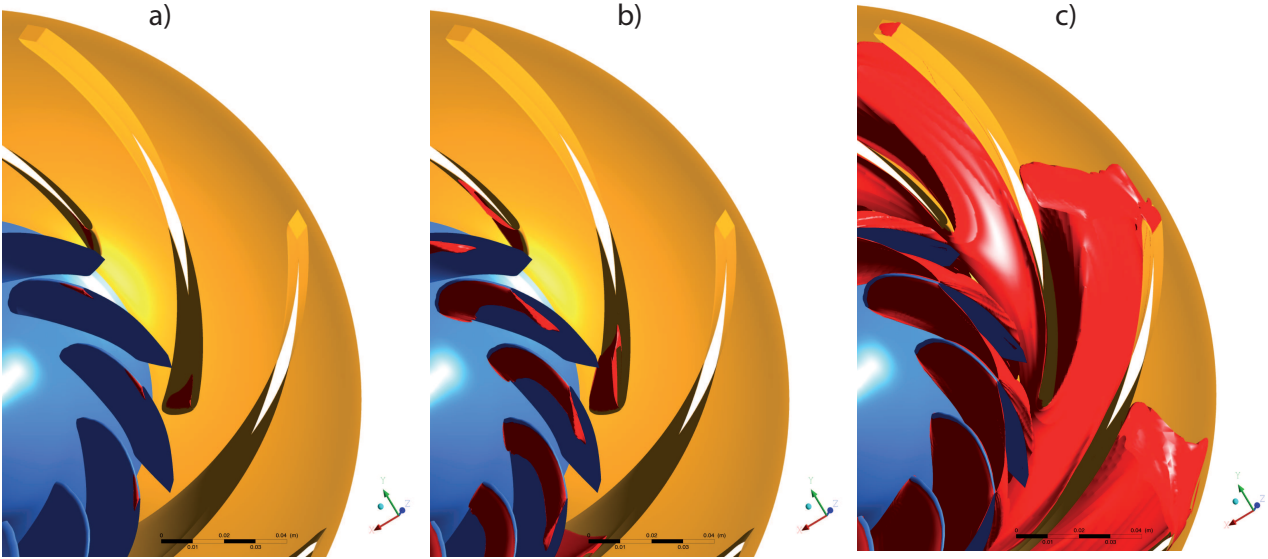

Figure 12: **CFD Cavitation Analysis of Prototype** $RoDiff_1$**: in red color the vapor volume fraction for different simulated inlet pressure at BEP a)** $50\%p_{(1),t}$**, b)** $20\%p_{(1),t}$**, c)** $15\%p_{(1),t} = NPSH_{3\%}$

cavitation takes place at SS of the FR as well as simultaneously at SS of RR and this unexpected phenomena needs to be proved by experimental measurements. It could be argued that the high relative speeds taking place at the SS of RR causes the cavitation by bringing the local wall static pressure lower than the vapor pressure. The cavitation starts from rotor tip and it propagates progressively by dropping inflow pressure until the hub. According with the CFD results the cavitation bubbles, which grow at the FR LE, are collapsed before reaching the TE as long that the inlet total pressure $p_{(1)t}$ remains higher than the reference value at $NPSH_A = 10m$. By a subsequent drop of the inlet pressure between 20% and 15%, the cavitation bubbles flow through the entire bladed passage collapsing at RR TE. Therefore, for developing the second prototype the authors worked on those velocity accelera-

tions to improve the cavitation behavior, by changing the blade circulation and thickness distributions. Furthermore the head drop curves of $RoDiff_1$ at 5 different discharges have been measured and presented in Figure 14. As usual running the NPSH-curve from right to left, the inlet total pressure $p_{(1)t}$ has to be reduced slowly by constant discharge and rotational speed. For each new value of $NPSH_A$ the correspondent head H is compared to the $H_{97\%}$. This is defined as 97% of the machine head in cavitation free working condition, in this conditions once the actual head H crosses the $H_{97\%}$ the $NPSH_{3\%}$ is defined. The accuracy of the results was affected by the presence of a gas leak in the inflow pipe line, small percentage (between 2% and 4% in volume) of air have been observed at suction side of the FR directly coming from the pipeline. This phenomena has been observed once the $NPSH_A$ value reaches 5 m, which corresponds to the system's absolute pressure of almost $50000 Pa$. Improvements on the test rig and its gas-tight characteristic is still under investigation. In addition to that an uncertainty must be considered while comparing CFD results.
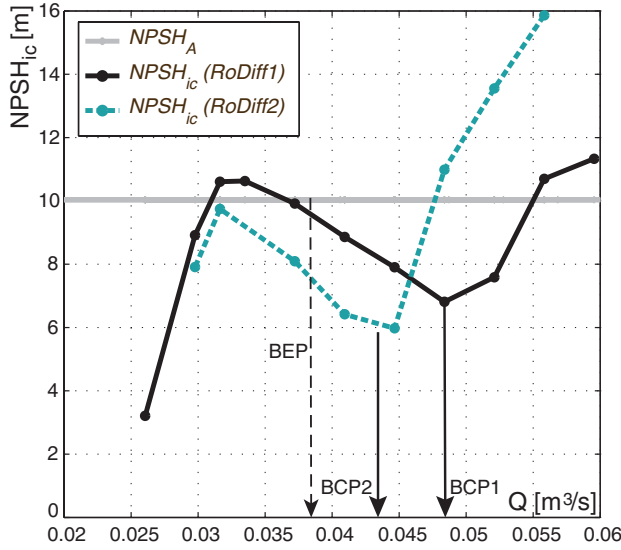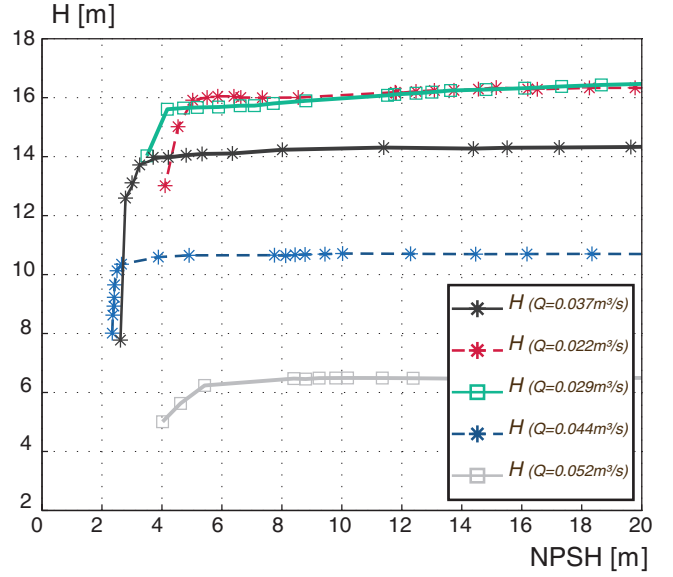

Figure 13: **Cavitation Inception Curves**

Figure 14: **Experimental head drop curves NPSH for several discharges,** $RoDiff_1$

Although the presence of the gas could be considered as one of the more significant reasons of the mismatch between CFD and EXP shown at Figure 15. Before starting to discuss about Figure 15, the results of the inception cavitation analysis in Figure 13 need to be highlighted. This CFD analysis has been done in single phase without activating the cavitation model. The definition of $NPSH_{ic}$ inception cavitation used below is given in Equation (6) above and as written it is valid as long that $NPSH_{ic} < NPSH_A$, see the work of Schiavello et al. (2009 [6]). Indeed without cavitation model the plotted points over the $NPSH_A$ line show just the trend but the values might be inaccurate. Figure 13 displays the NPSH inception curve of $RoDiff_1$ and $RoDiff_2$ and gives a clear comparison about the position of the Best Cavitation Point (BCP), also called shock-less point. The results confirm the improvements done by the re-design of $RoDiff_2$. The same conclusion could be achieved observing Figure 15, where the $NPSH_{3\%}$ of $RoDiff_2$ is also lower compared to $RoDiff_1$. Moreover the BCP is closer to the BEP in $RoDiff_2$ and its value is lower, although the cavitation free range is narrower. That actually is the effect of the blade LE thickness which has been reduced as mentioned. The authors argue that, in order to get a large cavitation free range, the speed ratio needs to be adapted to the changing flow conditions, as done in the previous Figure 10. The authors expect similar behavior once the speed ratio of the runners is progressively adjusted. A weakness of this design seems to be the flow instabilities at low capacity. Figure 15 reports clearly the appearing of the suction recirculation at quite high discharge, already by 80% of the design capacity.
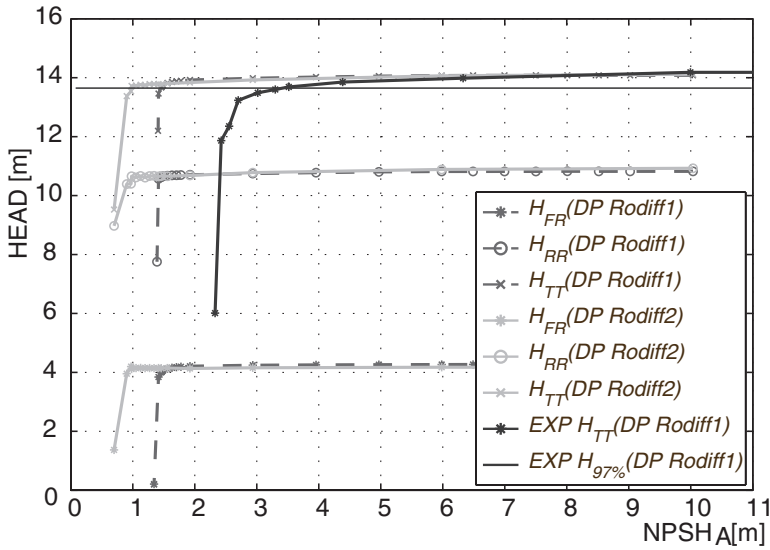
Figure 15: **Head Drop Curves at design capacity** Q

Furthermore observing the head rise curve at Figure 5 a positive slope is highlighted. The authors' point of view on this topic is that such a pump layout is intrinsically based on the impeller speed ratio adaptation, so that once the speed ratio is kept constant for a broad discharge range the system shows a sharp increase of the hydraulic losses, actually with a higher sensitivity than a regular pump. One of the main reasons, which has been identified, is the substantial increase of the LE incidence losses in part load capacity by double, which take place firstly at the FR LE and subsequently at RR LE. Finally the comparison between CFD and experimental measured head drop curve is given at Figure 15. The CFD value of $NPSH_{3\%}$ does not match properly the measurement. However the reason of this displacement is still under investigation. Most probably as already mentioned, the observed presence of gas bubbles within the main water flow at suction side flange is one of the causes of the mismatch. Additionally the Rayleigh-Plesset model used for the CFD analysis requires some experience values which have been left in the solver at default. At this point further investigation is planned, once the pipeline is gas-tight.

CONCLUSIONS

A preliminary numerical and experimental analysis on counter-rotating mixed-flow pumps has been presented. Several aspects have been investigated as: cavitation behavior, load distribution between the impellers and the system's sensitivity to the speed ratio. Moreover two new prototypes have been introduced and numerically compared to the actual tested design.

Goal of these analyses is to confirm the reliability of the in house developed design tool, based on CFD and analytical methodologies, with the experimental results. The comparisons suggest a substantial agreement with the CFD results, and validate the CFD optimization based development methodology, used in the presented study. It has been reported, that this new layout, e.g. prototype $RoDiff_1$, permits to extend the pump working range by adjusting progressively the speed ratio. While varying the load distribution between the rotors, different power density and pump characteristics can be achieved, e.g. prototype $RoDiff_3$. Finally the CFD analyses of the improved design $RoDiff_2$ with better cavitation behavior at BEP has been discussed. The CFD cavitation investigations do not match properly the experimental results due to gas leakage flowing into the water main flow at the test rig, the solution of this issue is still being investigated.

One of the most important considerations, which this study has suggested, is that the actual system requires an auto-adaptive speed ratio regulation to avoid performance instability in off-design. The speed ratio optimization is in other words not an improvement but a necessary adjustment to be able to exploit the potential of a counter-rotating mixed-flow pump. Finally it can be said that the present paper ensures a solid starting point for the future work. The intent of the authors is to use the actual design tool to re-design within the same spiral-duct a new layout for an even higher power density, by speeding up both impellers.

ACKNOWLEDGEMENTS

NOMENCLATURE

Symbols

a	Meridional coordinate [m]
C	Absolute velocity [m/s]
D	Diameter [m]
g	Gravity acceleration [m/s^2]
$H_{(i)}$	Impeller Design Head [m]
H_{RRVO}	Head increase within RR and VO[m]
M	Torque [Nm]
$n_{(i)}$	Rotor speed [rpm]
NPSH	Net Positive Suction Head [m]
$p_{(j)s}$	Static Pressure on position (j)[Pa]
$p_{(j)t}$	Total Pressure on position (j)[Pa]
p_v	Vapor Pressure [Pa]
P	Shaft Power [W]
Q	Volume flow rate [m^3/s]
T	Temperature [^oC]
U	Tangential velocity [m/s]
W	Relative velocity [m/s]
(x,y,z)	Cartesian coordinate system
(R,θ,Z)	Cylindrical coordinate system
$\beta_{b(j)}$	Blade angle[rad]
Γ	Circulation (Spring, 1992 [8])
χ	Blade obstruction factor [-]
χ_H	Load distribution factor [-]
$\omega_{(i)}$	Angular Velocity [rad/s]
η	Hydraulic Efficiency [-]
ρ	Water density [kg/m^3]
ρ_{imp}	Impeller material density[kg/m^3]
ρ_P	Power density [W/kg]

Abbreviations

BEP	Best Efficiency Point
BCP	Best Cavitation Point
CFD	Computational Fluid Dynamics
EXP	Experimental Results
LE	Blade Leading edge
PS	Blade Pressure Side
SS	Blade Suction Side
TE	Blade Trailing edge

Subscripts

1	Front rotor blade inlet
2	Front rotor blade outlet
2'	Section between FR and RR
3	Rear rotor blade inlet
4	Rear rotor blade outlet
4'	Section between RR and Volute
5	Volute inlet
6	Volute middle section
A	Available
atm	Atmospheric conditions
b	Blade
ic	Cavitation inception
i	Rotor index
j	Streamwise position index
FR	Front Rotor, Figure 2
e	Prototype number
m	Meridional component
RR	Rear Rotor, Figure 2
s	Static
t	Total
TT	Total to total magnitude
u	Tangential component
θ	Tangential component

References

[1] Ansys. *Ansys CFX User Manual*. ANSYS, Inc. Canonsburg PA, USA, release 14.5.7 edition, 2013.

[2] L. Cao, H. Honda, H. Yoshimura, S. Watanabe, and A. Furukawa. Experimental investigation of blade rows interactions in contrarotating axial flow pump. *Proceedings of 4th Joint US-European Fluids Engineering Summer Meeting, Chicago, Illinois, USA*, 2014.

[3] J. F. Guelich. *Kreiselpumpen Handbuch fuer Entwicklung, Anlagenplanung und Betrieb*. Springer Heidelberg Dordrecht London New York, 3 edition, 2010.

[4] T. Kanemoto and S. Oba. Proposition of unique pumping system with counter-rotating mechanism. *International Journal of Rotating Machinery, Volume 10 (2004), Issue 4, Pages 233-240, (http://dx.doi.org/10.1155/S1023621X04000259)*, 2004.

[5] S. Momosaki, S. Usami, S. Watanabe, and A. Furukawa. Numerical simulation of internal flow in a contra-rotating axial flow pump. *25th IAHR Symposium on Hydraulic Machinery and Systems, IOP Conf. Series: Earth and Environmental Science 12 012046 , (doi:10.1088/1755-1315/12/1/012046)*, 2010.

[6] B. Schiavello and F. C. Visser. Pump cavitation various npshr criteria, npsha margins and impeller life expectancy. *Proceedings of 25th International Pump User Symposium*, 2009.

[7] T. Shigemitsu, A. Furukawa, S. Watanabe, K. Okuma, and J. Fukutomi. Experimental analisys of internal flow of contra-rotating axial flow pump. *International Symposium on Experiemntal and Computational Aerothermodynamics of Internal Flows*, 2007.

[8] H. Spring. Affordable quasi three-dimensional inverse design method for pump impellers. *Proceeding of the ninth International Pump Users Symposium*, pages 97–110, 1992.

[9] S. Tosin. New approach for multi-rotor mixed-flow pump design and optimization. *Proceedings of 4th Joint US-European Fluids Engineering Summer Meeting, Chicago, Illinois, USA, FEDSM2014-21595*, 2014.

[10] J. Wang, F. Ravelet, and F. Bakir. Influence of design parameters on the global performances of low-speed counter-rotating axial-flow fans. *Proceedings of 4th Joint US-European Fluids Engineering Summer Meeting, Chicago, Illinois, USA, FEDSM2014-22172*, 2014.